Current Applied Physics 85 (2026) 103–110

Contents lists available at ScienceDirect

Current Applied Physics

journal homepage: www.elsevier.com/locate/cap

High-performance and durable PEDOT:PSS/$LaVO_3$ flexible semitransparent solar cells with graphene quantum dots

Bo Gyu Choi [a,1], Dong Hee Shin [b,1], Hosun Lee [a,*]

[a] Department of Applied Physics, Kyung Hee University, Yongin, 17104, Republic of Korea
[b] Department of Smart Sensors Engineering, Kyungkuk National University, Andong, Gyeongbuk, 36729, Republic of Korea

ARTICLE INFO

Keywords:
$LaVO_3$
Graphene quantum dots
PEDOT:PSS
Semitransparent photovoltaics
Long-term stability
Mechanical durability

ABSTRACT

Flexible and semitransparent solar cells are emerging as promising solutions for wearable devices and building-integrated photovoltaics. Here, we demonstrate for the first time a PEDOT:GQDs/$LaVO_3$ heterojunction solar cell that combines the strong light absorption of $LaVO_3$ with the improved conductivity and interface stability provided by PEDOT:PSS containing GQDs. The GQDs concentration was systematically varied to identify the optimal condition, and as a result, the device with 10 mg/L GQDs achieved a power conversion efficiency of 4.84%, significantly higher than that of the pristine device. In addition, an Al back reflector further enhanced light harvesting, improving efficiency to 5.35%, i.e. about 10% increase in relative efficiency. The solar cell showed a 39% drop from its initial efficiency after 2000 h under ambient conditions (30 °C and 40-45% relative humidity) and less than 14% degradation after 3000 bending cycles (curvature radius of 4 mm), confirming excellent long-term and mechanical stability. These results highlight the strong potential of the PEDOT:GQDs/$LaVO_3$ architecture for reliable and efficient flexible photovoltaic applications.

1. Introduction

In recent years, flexible and semitransparent solar cells have emerged as promising candidates for next-generation wearable electronics, portable power sources, building-integrated photovoltaic applications, and vehicle sunroofs [1–5]. These devices are especially attractive because they can deliver both daylighting and energy harvesting, offering high space efficiency and straightforward integration into existing structures and consumer products [6,7]. Accordingly, developing lightweight and flexible semitransparent photovoltaics with versatile design options has become an important research direction.

Among various absorber materials, $LaVO_3$ has emerged as an attractive candidate due to its high optical absorption from the ultraviolet (UV) to the visible region, which allows for efficient light harvesting even with thin films [8–12], making it well suited for lightweight and flexible photovoltaic applications. To further improve the performance of $LaVO_3$-based devices, it is essential to adopt an effective hole transport layer (HTL) that ensures high conductivity, excellent optical transparency, and good mechanical compatibility with flexible substrates. Poly(3,4-ethylenedioxythiophene):poly(styrenesulfonate) (PEDOT:PSS) has been widely used as an HTL because of its advantages such as antireflection, interface passivation, facilitation of hole transport, and good optical transmittance [13–16]. However, the inherently low conductivity of PEDOT:PSS can limit the power conversion efficiency (PCE) and long-term device stability [17–19]. To overcome this limitation, carbon-based nanomaterials such as graphene quantum dots (GQDs) have recently been introduced to improve the electrical conductivity, carrier mobility, and chemical stability of PEDOT:PSS [20–22]. In our previous study, we demonstrated PEDOT:GQDs/porous Si solar cells that exhibited enhanced efficiency following the incorporation of GQDs [23]. However, the inherent rigidity of Si-based substrates limits their application in semitransparent and flexible photovoltaics. In contrast, $LaVO_3$ films integrated onto flexible substrates facilitate semitransparent operation while maintaining mechanical flexibility. Consequently, incorporating GQDs into PEDOT:PSS is expected to significantly improve the power conversion efficiency and durability of these flexible solar cells.

Here, we first report a flexible and semitransparent solar cell based on a PEDOT:GQDs/$LaVO_3$ heterojunction structure and systematically analyze its photovoltaic parameters as a function of GQDs concentration. In addition, to confirm its practical feasibility as a flexible solar cell, both long-term stability and mechanical stability were evaluated.

* Corresponding author.
E-mail address: hlee@khu.ac.kr (H. Lee).
[1] The two authors contributed equally to this work.

https://doi.org/10.1016/j.cap.2026.02.001
Received 20 August 2025; Received in revised form 8 January 2026; Accepted 4 February 2026
Available online 6 February 2026

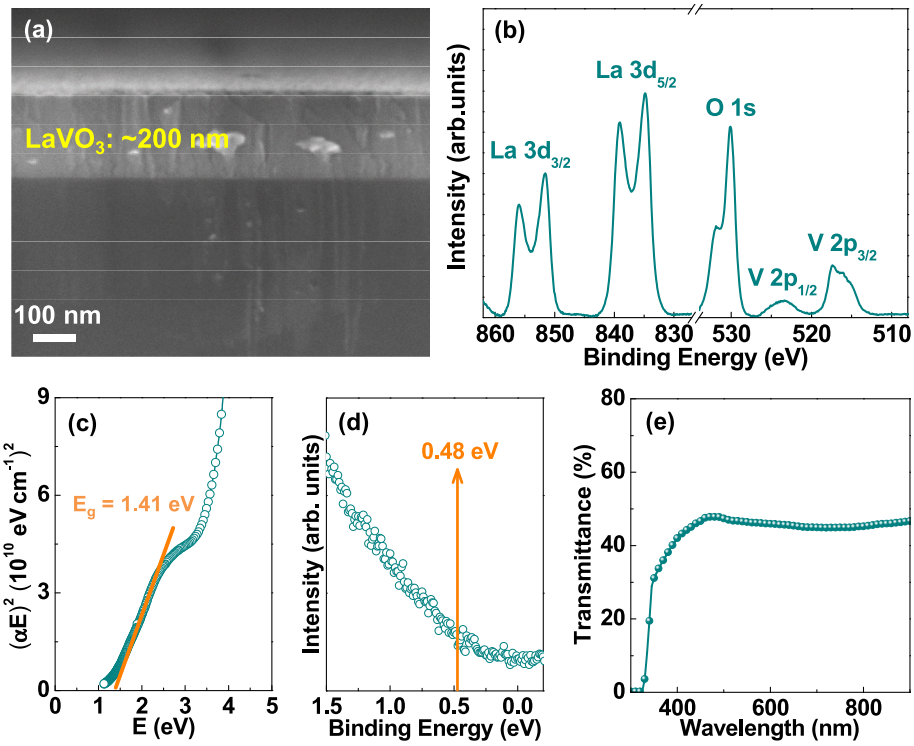

Fig. 1. (a) Cross-sectional SEM image of the $LaVO_3$ thin film. (b) Its corresponding XPS spectrum. (c)-(d) Optical bandgap energy derived from spectroscopic ellipsometry and UPS spectrum measured on a $LaVO_3$/Si sample. (e) Optical transmittance spectrum of the $LaVO_3$ film measured on a PET substrate.

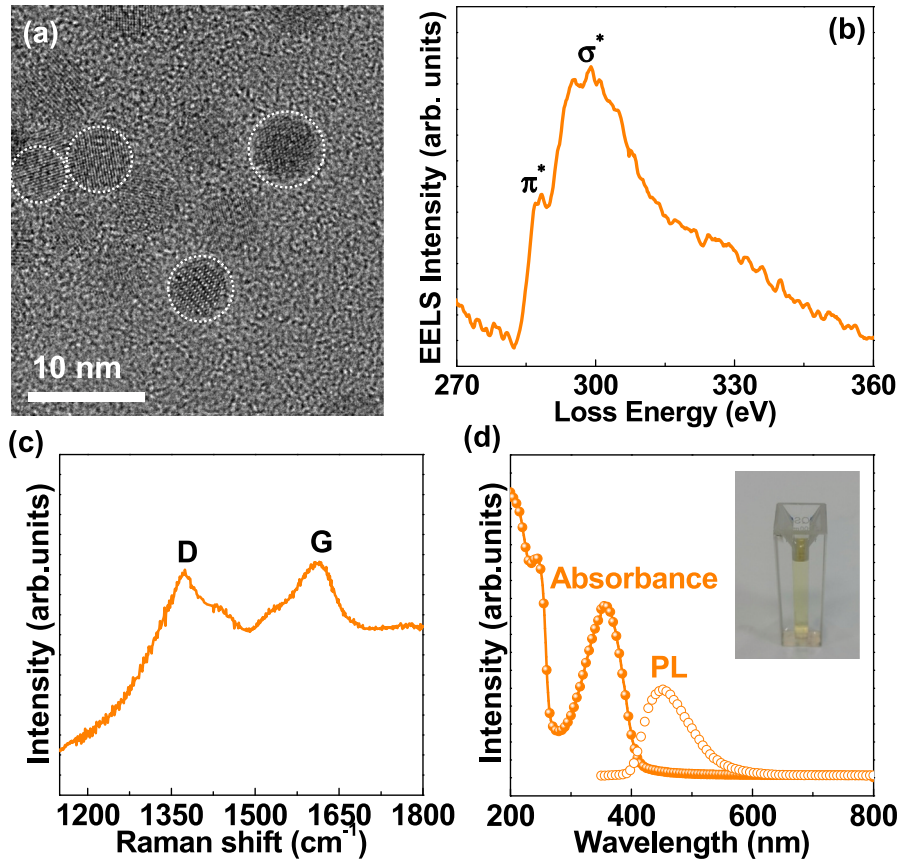

Fig. 2. (a) TEM image, (b) EELS spectrum, (c) Raman spectrum, and (d) UV–vis absorbance spectrum of the GQDs. The inset in (d) shows a photograph of the GQD solution.

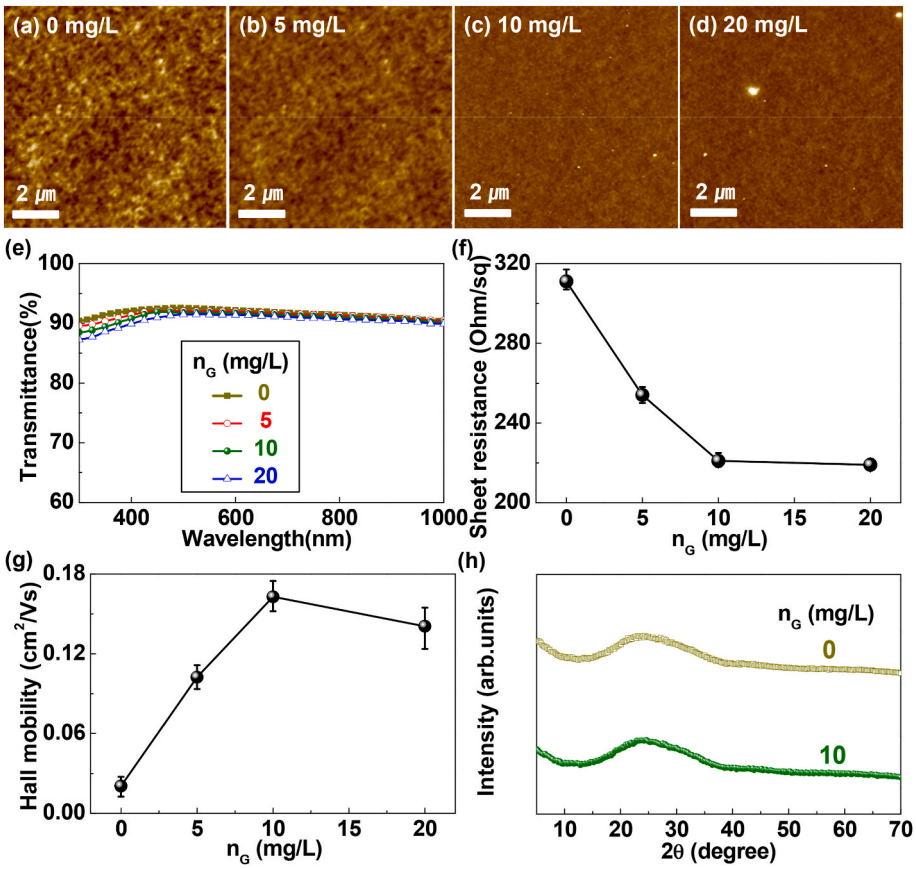

Fig. 3. n_G-dependent AFM image of PEDOT:GQDs. (a) 0, (b) 5, (c) 10, and (d) 20 mg/L. (e) Transmittance, (f) Sheet resistance, and (g) Hall mobility of the PEDOT:GQDs for various n_G. (h) XRD patterns of PEDOT:GQDs for n_G = 0 and 10 mg/L.

2. Experimental section

2.1. Fabrication of PEDOT:GQDs/$LaVO_3$ solar cell

Prior to deposition, the PET substrate was sequentially cleaned in ultrasonic baths of acetone, ethanol, and deionized water, and then dried with N_2 gas. Simultaneously, pre-sputtering of the $LaVO_3$ target was performed to stabilize the chamber conditions. Subsequently, the $LaVO_3$ thin film was deposited onto the PET substrate at room temperature using RF magnetron sputtering of a $LaVO_3$ target at a power of 100 W under a mixed gas atmosphere of 35% H_2 and Ar. GQDs with an average diameter of approximately 5 nm were first dispersed into a PEDOT:PSS solution (Clevios PH 1000). The resulting PEDOT:GQDs composite solutions were prepared with defined GQDs concentrations (n_G) ranging from 5 to 20 mg/L. The concentration was controlled by adjusting the amount of added GQDs powder. The resulting mixture was spin-coated onto the $LaVO_3$ film at 3000 rpm for 40 s and thermally annealed at 100 °C for 30 min. The device was completed by depositing Au and Ag films as the top and bottom electrodes, respectively.

2.2. Characterizations

The thickness of the $LaVO_3$ thin films was examined using field-emission scanning electron microscopy (FE-SEM, Carl Zeiss, LEO SUPRA 55). The atomic bonding states of $LaVO_3$ and GQDs were analyzed by X-ray photoelectron spectroscopy (XPS) employing an Al *Kα* source (1486.6 eV). The morphology and size distribution of the GQDs were investigated using high-resolution transmission electron microscopy (HRTEM, JEOL model JEM-2100F) coupled with electron energy loss spectroscopy (EELS) mapping. To further verify the presence of GQDs, absorbance, photoluminescence (PL), and Raman spectra were measured. The sheet resistance of the PEDOT:GQDs films was measured using the four-probe van der Pauw method (Dasol eng., model FPPHS8-40K). Transmittance spectra (Varian, model Cary 5000) and X-ray diffraction (XRD) patterns were recorded to compare the optical and structural properties of PEDOT:PSS and PEDOT:GQDs films. To perform Hall-effect measurements, PEDOT:GQDs films were prepared on quartz substrates under identical fabrication conditions. The electrical properties were evaluated as a function of GQD concentration using a Hall measurement system (Ecopia, HEM-2000) employing the van der Pauw configuration. To establish Ohmic contacts, indium electrodes with a diameter of 500 μm were deposited onto the films via thermal evaporation through a shadow mask, followed by post-deposition annealing at 100 °C for 20 min. During the measurements, a magnetic field of 0.37 T was applied, while the current was varied from 0.1 μA to 10 mA. All characterization was conducted under dark conditions to eliminate any influence from ambient light. The photovoltaic parameters of the device were characterized by measuring the current density–voltage (*J*–*V*) curves under standard AM 1.5G solar illumination (100 mW/cm^2) using a Keithley 2400 source meter under ambient conditions. The external quantum efficiency (EQE) was evaluated across the wavelength range of 300 to 1000 nm using a monochromator-equipped white light source. To investigate the evolution of device efficiency under mechanical stress, we performed 3000 repeated bending cycles at a curvature radius of 4 mm and a frequency of 0.5 Hz.

3. Results and discussion

Fig. 1(a) reveals that the $LaVO_3$ film exhibits a uniform morphology with a thickness of approximately 200 nm. Fig. 1(b) shows the XPS spectra of the $LaVO_3$ film, showing distinct binding energies corresponding to La 3d, O 1s, and V 2p. The spin–orbit splitting observed

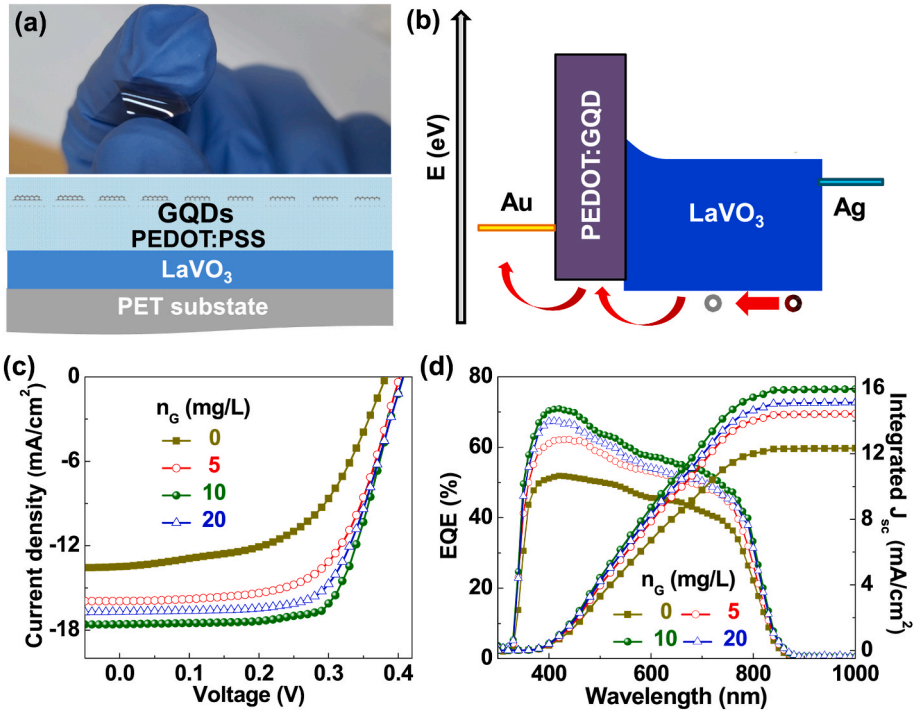

Fig. 4. (a) Schematic and (b) energy band diagram of a typical PEDOT:GQDs/$LaVO_3$ solar cell. (c) *J–V* curves under 1sun illumination and (d) EQE/integrated J_{sc} spectra.

between the La 3d and V 2p main peaks indicates that the La/V atomic ratio is close to the stoichiometric composition of $LaVO_3$ [24]. The optical bandgap energy of $LaVO_3$ is estimated to be 1.41 eV, based on Tauc plot extrapolation of the absorption coefficient, as shown in Fig. 1(c). Using scanning Kelvin probe and UPS analyses, the Fermi level (E_F) and valence band maximum (E_v) of $LaVO_3$ were evaluated to be 4.87 and 5.35 eV, respectively, as illustrated in Fig. 1(d). Fig. 1(e) shows that the $LaVO_3$/PET structure exhibits more than 45% transmittance in the visible region. This result indicates its suitability for semitransparent device applications.

Fig. 2(a) shows low-magnification TEM images illustrating the overall dispersion of the GQDs, demonstrating that their average size is approximately 5 ± 2.2 nm, where the average size was defined as half of the sum of the width and length of an individual GQD. In Fig. 2(b), the carbon K-edge EELS spectrum obtained from the same region as the HRTEM image shows distinct peaks at approximately 285 and 291 eV. These peaks correspond to the π* and σ* electronic states, which are attributed to the sp^2 carbon domains present in the GQDs [25]. As shown in Fig. 2(c), the Raman spectrum of the GQDs exhibits well-defined D and G peaks, consistent with previous studies [26]. Fig. 2(d) illustrates the down-conversion behavior of the GQDs, which absorb UV light and emit in the visible region. Absorbance and PL peaks appear at 356 nm and 450 nm, respectively [27,28].

Fig. 3(a)–(d) shows the AFM analysis of the surface morphology of PEDOT:GQDs films with varying n_G. The surface roughness exhibited only a slight variation, increasing from 2.49 to 3.95 nm with increasing n_G. This suggests that the n_G affects the film's surface features only slightly. Fig. 3(e) presents the transmittance spectra of PEDOT:PSS films as a function of n_G. The transmittance at 550 nm and the average visible transmittance (AVT) across the 400–800 nm range remained largely unchanged with varying n_G. In contrast, the transmittance in the 300–400 nm region gradually decreased with increasing n_G, which is attributed to the GQDs absorbing light in the UV region. Fig. 3(f) shows that the sheet resistance of PEDOT:PSS/$LaVO_3$ gradually decreased from approximately 311 ± 6 to 219 ± 3 Ω/sq as n_G increased. Fig. 3(g) illustrates the hole mobility of PEDOT:GQDs as a function of n_G. As n_G increases up to 10 mg/L, the hole mobility of the PEDOT:GQDs is markedly enhanced, suggesting that the incorporation of GQDs facilitates charge-carrier hopping along the PEDOT chains. When the GQD concentration exceeds 10 mg/L, the hole mobility begins to decline; however, it remains higher than that of the pristine film. This behavior suggests that excessive GQD loading leads to a degradation of the optimized conductive network rather than its complete disruption, thereby resulting in reduced mobility [20,29].

The similar XRD patterns of PEDOT:PSS and PEDOT:GQDs suggest that GQDs have little impact on the polymer's crystalline structure, as shown in Fig. 3(h).

Fig. 4(a) shows the real image/schematic diagram of PEDOT:GQDs/$LaVO_3$ on the flexible substrate. Fig. 4(b) shows the energy band structure of the PEDOT:GQDs/$LaVO_3$ device. Upon illumination, photogenerated electrons and holes are generated in the $LaVO_3$ region and are efficiently transported toward the Ag and Au electrodes, respectively. PEDOT:PSS blended with graphene oxide is known to exhibit a benzoid–quinoid structural transition, resulting in an increase in the material's work function [30]. Therefore, the work function of PEDOT:GQDs is assumed to be higher than that of PEDOT:PSS, consistent with

Table 1
Photovoltaic parameters and electrical characteristics of PEDOT:GQDs/$LaVO_3$ solar cells with varying n_G.

n_G (mg/L)	V_{oc} (V)	J_{sc} (mA/cm^2)	FF (%)	PCE (%)	R_{sh} (Ω-cm^2)	R_s (Ω-cm^2)	*n*	τ_{rise} (μs)	τ_{decay} (μs)	Gain
0	0.367	21.61	54.10	2.77	4173	5.49	3.73	272	423	1.56
5	0.456	28.74	62.00	3.95	5062	4.02	3.18	248	698	2.81
10	0.483	29.86	67.11	4.84	5737	2.68	2.84	232	890	3.84
20	0.508	32.75	65.42	4.42	5469	2.81	2.96	239	845	3.54

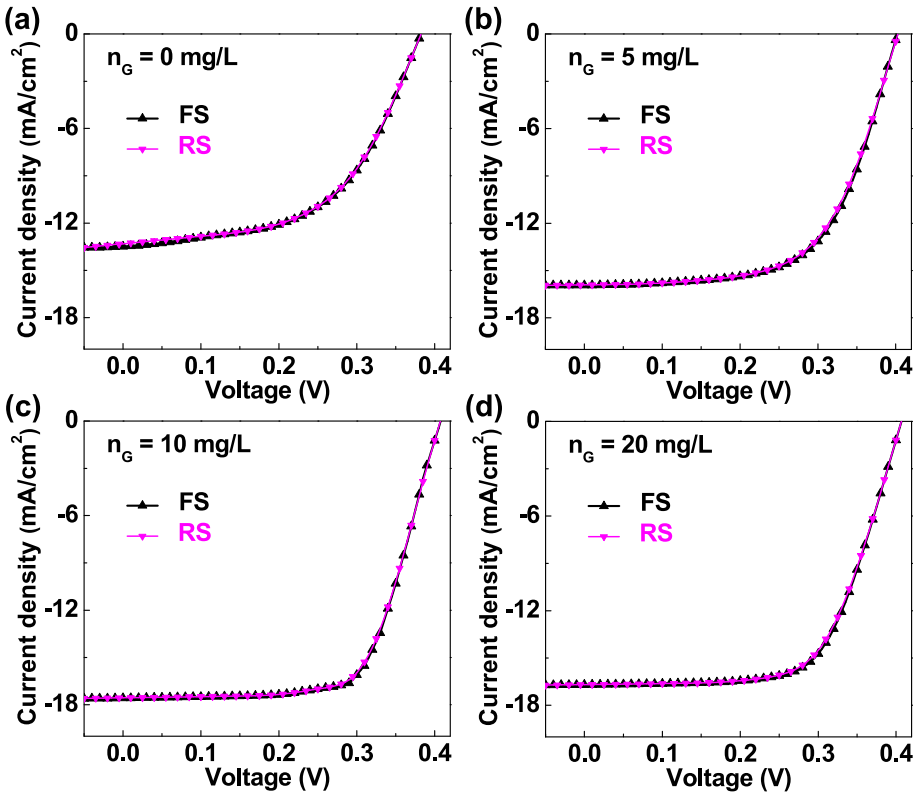

Fig. 5. *J–V* curves at the forward scan (FS) and reverse scan (RS) conditions of PEDOT:GQDs/$LaVO_3$ solar cells with different n_G.

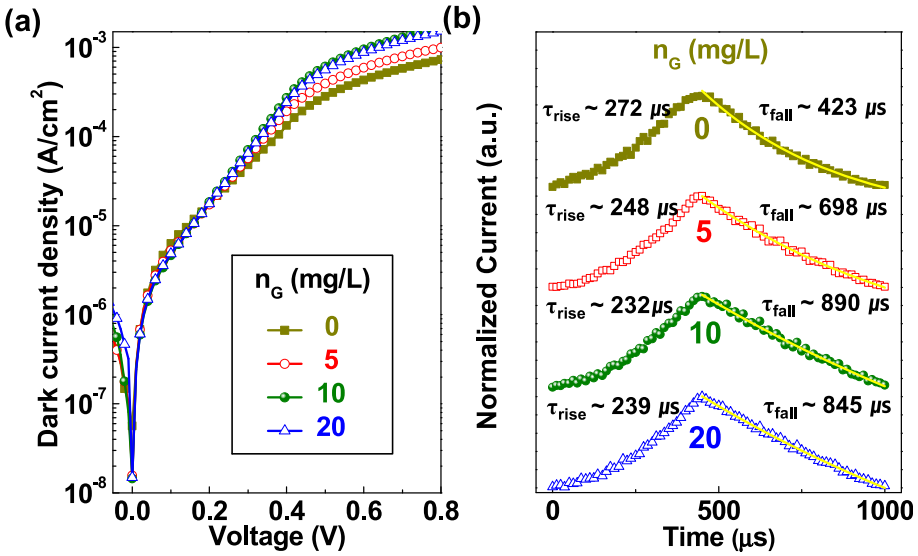

Fig. 6. (a) Dark I–V curves of PEDOT:GQDs/$LaVO_3$ solar cells as a function of n_G. The curves are divided into low- (<0.1 V), intermediate- (0.1–0.4 V), and high-voltage (>0.4 V) regions for analysis. (b) Normalized transient photocurrent responses under pulsed 532 nm laser excitation with varying n_G.

the benzoid–quinoid transition mechanism [31,32]. GQDs are generally surrounded by highly oxidized functional groups [33,34], and the observed increase in work function upon adding GQDs to PEDOT:PSS can therefore be attributed to this structural transition. In the PEDOT:GQDs/$LaVO_3$ structure, the improved energy-level alignment can reduce the interfacial energy barrier and enhance charge extraction efficiency. Consequently, PEDOT:GQDs-based $LaVO_3$ devices are expected to demonstrate enhanced performance.

Fig. 4(c) exhibits the *J-V* characteristics of the solar cells measured under 100 mW cm^{-2} for various n_G. The control device without GQDs showed an open-circuit voltage (V_{oc}) of 0.380 V, a short-circuit current density (J_{sc}) of 13.49 mA/cm^2, a fill factor (FF) of 54.10%, and a power conversion efficiency (PCE) of 2.77 %. The PEDOT:GQDs/$LaVO_3$ device exhibited a maximum PCE of 4.84%, a V_{oc} of 0.410 V, a J_{sc} of 17.58 mA/cm^2, and an FF of 67.11% at n_G = 10 mg/L, as summarized in Table 1. The PCE slightly decreased to 4.42% at n_G = 20 mg/L. This is considered to result from disrupted charge transport or increased recombination caused by excessive GQDs. These results can be explained by an optimized GQDs loading that enhances hole mobility and charge extraction efficiency without damaging the PEDOT conductive network.

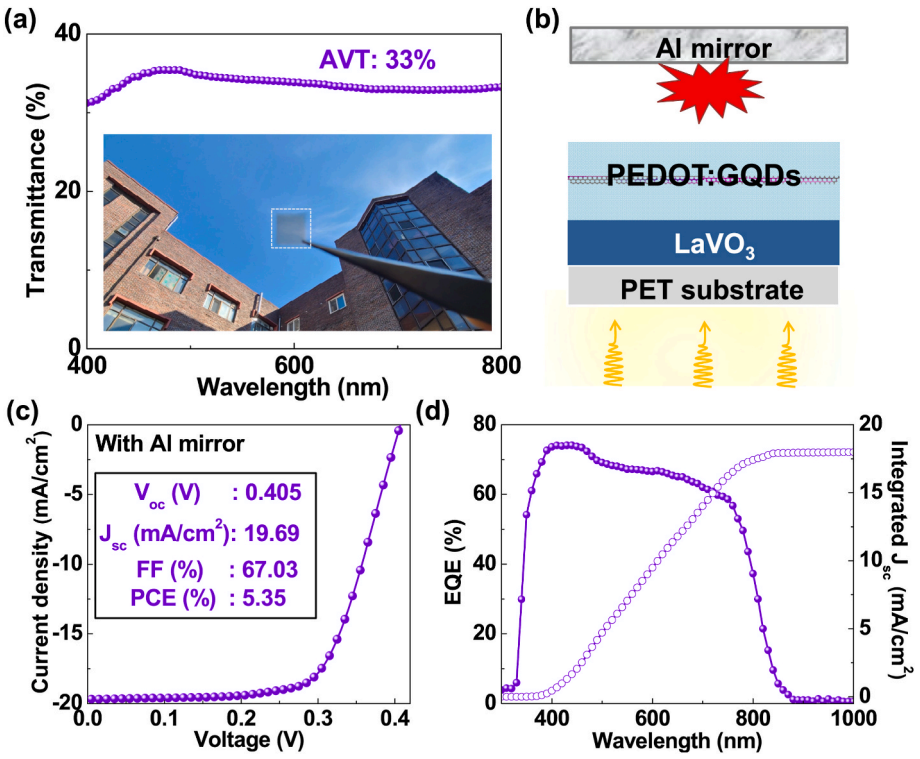

Fig. 7. (a) Optical transmittance spectrum of a representative PEDOT:GQDs/$LaVO_3$ at $n_G = 10$ mg/L. The inset shows photographs of the semitransparent device. (b) Schematic diagram of a semitransparent solar cell with Al reflective mirror. (c) *J-V* curves of the semitransparent cell with an Al reflective mirror under illumination from the PEDOT:GQDs side. (d) EQE spectra of devices with Al mirror.

Fig. 4(d) presents the EQE spectra and integrated J_{sc} over the 300–1000 nm wavelength range for various n_G. While optical transmittance decreases with increasing GQD concentration, J_{sc} does not follow the same trend, suggesting that the short-circuit current is not governed solely by transmittance. Instead, J_{sc} is primarily determined by the visible-light absorption of $LaVO_3$ and the charge transport properties of the PEDOT:GQDs layer. At $n_G = 10$ mg/L, improvements in charge transport—specifically enhanced hole mobility and reduced sheet resistance—outweigh the optical losses. This yields the highest EQE across the measured spectral range, which is in good agreement with the integrated J_{sc} [35].

Fig. 5(a)–(d) illustrate the forward and reverse *J–V* characteristics of the fabricated devices. No significant *J–V* hysteresis was observed within the measurement resolution, indicating stable charge transport and ensuring a reliable evaluation of photovoltaic performance. This negligible hysteresis is attributed to the relatively simple heterojunction structure and efficient charge extraction at the PEDOT:GQDs/$LaVO_3$ interface.

To evaluate the enhanced performance of n_G-dependent devices, the shunt resistance (R_{sh}), ideality factor (*n*), and series resistance (R_s) were determined from the dark I–V characteristics, as presented in Fig. 6(a). The behavior of the I–V curves is generally governed by different parameters depending on the voltage range: R_{sh} dominates in the range of $V < 0.1$ V, the *n* becomes the main influence between 0.1 and 0.4 V, and R_s primarily affects the behavior when $V > 0.4$ V [36]. From the I–V curves, R_{sh} reached its maximum value of 5737 Ω cm^2 and R_s was minimized to 2.68 Ω cm^2 at $n_G = 10$ mg/L. Achieving a high FF requires a large R_{sh} and a low R_s. An increase in R_{sh} effectively suppresses interfacial recombination [37], while a lower R_s enables efficient charge extraction, leading to enhanced photovoltaic performance including FF, consistent with Table 1. Generally, higher hole mobility facilitates efficient carrier extraction; however, V_{oc} is not determined by mobility alone and is also significantly influenced by recombination characteristics and interfacial properties. While the maximum V_{oc} is observed at $n_G = 20$ mg/L, the device with $n_G = 10$ mg/L exhibits an optimal balance between hole mobility and series resistance (R_s). This optimization leads to substantial improvements in J_{sc} and FF, thereby yielding the highest overall PCE.

Additionally, the *n* was extracted using the equation: $J = J_s [\exp(eV/nkT) - 1]$ [38,39], where J_s represents the reverse saturation current density, k_B is the Boltzmann constant, and T is the absolute temperature. Consequently, the *n* of the device with $n_G = 10$ mg/L was evaluated to be 2.84, implying reduced electron-hole recombination, thereby leading to good diode characteristics.

The transient photocurrent (PC) responses were also evaluated under different n_G. Here, the rise time is defined as the time required for photogenerated carriers within the $LaVO_3$ film to be swept out by the built-in electric field of the PEDOT:GQDs/$LaVO_3$ structure. Fig. 6(b) shows the transient PC responses measured as a function of n_G. Here, the rise time denotes the time required for photogenerated carriers within the $LaVO_3$ film to be swept out by the built-in electric field of the PEDOT:GQDs/$LaVO_3$ structure. Conversely, the decay time reflects the carrier lifetime. To extract this value, a single-exponential decay model was used: $R(t) = A_1 \exp(-t/\tau_1) + y_0$ [40], where τ represents the radiative recombination lifetime. From the model equation, the ratio of decay time to rise time was used to evaluate the carrier collection efficiency. At $n_G = 10$ mg/L, the rise and decay times were measured to be 232 and 890 μs, respectively, resulting in the highest collection efficiency of 3.84. The rise and decay times for other n_G values are summarized in Table 1. Overall, these findings confirm that the introduction of $n_G = 10$ mg/L significantly enhances the photovoltaic efficiency.

To evaluate the characteristics of the semitransparent device, we conducted a further investigation under the condition of $n_G = 10$ mg/L, which exhibited the highest efficiency. Fig. 7(a) shows a schematic of the device with an Al reflective mirror. To explore the potential of the semitransparent structure, the transmittance spectrum of the PEDOT:GQDs/$LaVO_3$ device was measured. As shown in Fig. 7(b), the average visible transmittance (AVT) in the 400–800 nm range was determined to

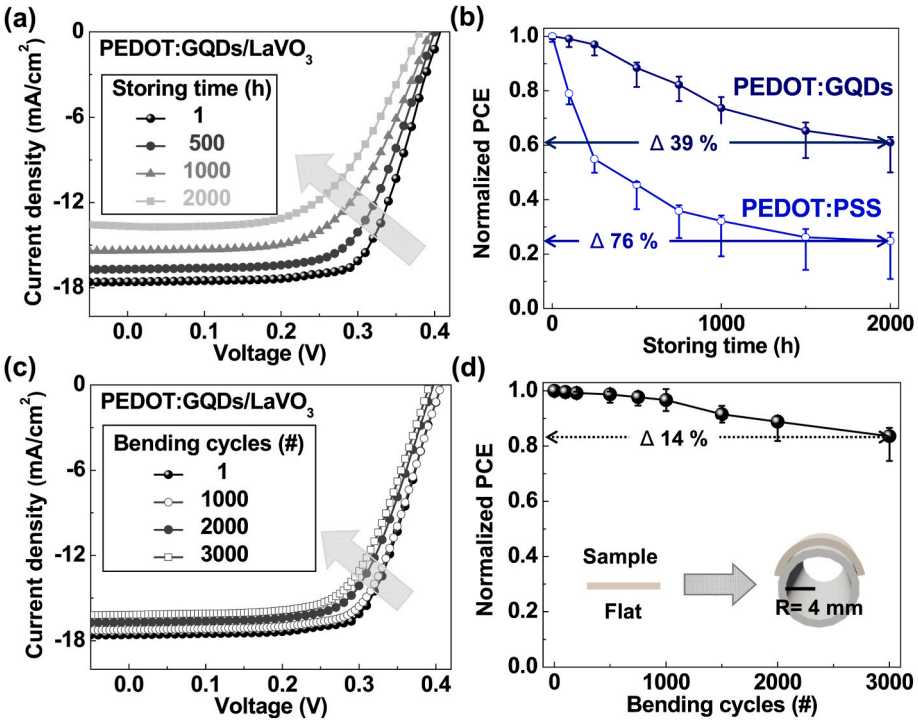

Fig. 8. Evolution of (a) *J-V* curve for cell with $n_G = 10$ mg/L. (b) Normalized PCE of the PEDOT:GQDs/$LaVO_3$ solar cell with $n_G = 0$ and 10 mg/L under ambient conditions (30°C and 40-45 % humidity) for 2000 h. (c) Change in *J–V* characteristics of the device with $n_G = 10$ mg/L after repeated bending up to 3000 cycles. (d) Normalized PCE versus the number of bending cycles; the inset illustrates the bending test setup with a radius of 4 mm.

be approximately 35%. Fig. 7(c) displays the *J–V* curves of the device with/without the Al reflector. As a result, the PCE of the PEDOT:GQDs/$LaVO_3$ device increased to 5.35% with the Al mirror, representing about a 10% improvement compared to the configuration without the mirror.

Fig. 7(d) shows the EQE spectra of the devices with the Al mirror. The integrated J_{sc} were 17.89 mA/cm^2, respectively, confirming an enhanced EQE across the broad wavelength range of 350–800 nm in the presence of the Al mirror. This improvement clearly demonstrates that the Al mirror effectively enhances light-harvesting, leading to a significant increase in J_{sc}.

The long-term stability of PEDOT:GQDs/$LaVO_3$ devices at $n_G = 0$ and 10 mg/L was comparatively evaluated based on the time-dependent evolution of their *J–V* characteristics (Fig. 8(a)–(b)). The storage temperature was maintained at 30 °C to simulate typical indoor ambient conditions. The devices were stored under dark conditions, except during intermittent *J–V* measurements.

Both devices were stored under identical ambient conditions (30 °C and 40-45% relative humidity), and their photovoltaic performance was measured under 1 sun illumination (100 mW cm^{-2}). After 2000h, the PEDOT:GQDs/$LaVO_3$ device retained approximately 61 % of its initial PCE, while the PEDOT:PSS/$LaVO_3$ device exhibited a more significant degradation, maintaining only about 24 % of its initial efficiency. This result indicates that introducing GQDs into PEDOT:PSS mitigates the hygroscopic and acidic properties of the PSS component. Conventional PEDOT:PSS readily absorbs moisture from the air, leading to an increase in sheet resistance and, consequently, a deterioration in device stability [41,42]. The low acidity of GQDs effectively suppresses interfacial degradation and maintains charge transport stability, thereby enhancing the durability of the device.

To further evaluate the mechanical stability, repeated bending tests were conducted on the PEDOT:GQDs/$LaVO_3$ with $n_G = 10$ mg/L at a curvature radius of 4 mm for up to 3000 cycles, as shown in Fig. 8(c). Fig. 8(d) shows that The PCE decreased slightly from 4.83% for the initial measurement to 4.04% after 3000 bending cycles, demonstrating excellent mechanical robustness. This excellent flexibility is attributed to the improved film uniformity and enhanced mechanical robustness induced by the GQDs. These findings confirm that the PEDOT:GQDs/$LaVO_3$ device is a promising candidate for flexible optoelectronic applications due to its excellent long-term and mechanical stability.

4. Conclusions

We demonstrated a flexible solar cell based on a PEDOT:GQDs/$LaVO_3$ heterojunction structure. The device with $n_G = 10$ mg/L exhibited a significant improvement in PCE, achieving a maximum of 4.84%, whereas the pristine device showed only 2.77%. The improved performance is attributed to the appropriate addition of GQDs, resulting in reduced series resistance, enhanced carrier mobility, increased optical transmittance, and lowered sheet resistance. Furthermore, the Al back reflector improved light harvesting efficiency from 4.84 to 5.35% by approximately 10%, which was attributed to the semitransparent property of the device. The device with $n_G = 10$ mg/L exhibited excellent long-term stability, with its efficiency decreasing by only 39 % compared to the initial PCE after 2000 h under ambient conditions. Moreover, the device showed excellent mechanical durability, exhibiting only a 14% decrease from its initial efficiency even after 3000 bending cycles. These results confirm that the PEDOT:GQDs/$LaVO_3$ structure not only improves photovoltaic performance but also ensures environmental and mechanical reliability, making it a promising candidate for flexible and semitransparent optoelectronic applications.

Declaration of competing interest

☑ The authors declare that they have no known competing financial interests or personal relationships that could have appeared to influence the work reported in this paper.

Acknowledgments

This work was supported by the National Research Foundation of

Korea (NRF) grant funded by the Ministry of Science, ICT & Future Planning: NRF-2021R1F1A1045446 (H. LEE) and NRF-2022R1C1C1008499 (D.H. SHIN).

References

[1] W. Liu, Y. Liu, Z. Yang, C. Xu, X. Li, S. Huang, J. Shi, J. Du, A. Han, Y. Yang, G. Xu, J. Yu, J. Liang, J. Peng, L. Yu, B. Ding, Y. Gao, K. Jiang, Z. Li, Y. Yang, Z. Li, S. Lan, H. Fu, B. Fan, Y. Fu, W. He, F. Li, X. Song, Y. Zhou, Q. Shi, G. Wang, L. Guo, J. Kang, X. Yang, D. Li, Z. Wang, J. Li, S. Thoroddsen, R. Cai, F. Wei, G. Xing, Y. Xie, X. Liu, L. Zhang, F. Meng, Z. Di, Z. Liu, Flexible solar cells based on foldable silicon wafers with blunted edges, Nature 617 (2023) 717.

[2] Y. Sun, F. Li, H. Zhang, W. Liu, Z. Wang, L. Mao, Q. Li, Y. He, T. Yang, X. Sun, Y. Qian, Y. Ma, L. Zhang, J. Du, J. Shi, G. Wang, A. Han, N. Wang, F. Meng, Z. Liu, M. Liu, Flexible perovskite/silicon monolithic tandem solar cells approaching 30% efficiency, Nat. Commun. 16 (2025) 5733.

[3] H. Lee, S. Jeong, J.-H. Kim, Y.-R. Jo, H.J. Eun, B. Park, S.C. Yoon, J.H. Kim, S.-H. Lee, S. Park, Ultra-flexible semitransparent organic photovoltaics, npj Flex. Electron. 7 (2023) 27.

[4] Z. Wu, B. Shi, J. Yu, M. Sha, J. Sun, D. Jiang, X. Liu, W. Yu, Y. Tan, H. Li, S. Huang, J. Wang, J. Liu, C. Zhang, X. Ma, L. Cui, L. Ye, F. Zhang, B. Cao, Y. Chen, Z. Ji, F. Chen, X. Hao, G. Li, H. Yin, Human-friendly semitransparent organic solar cells achieving high performance, Energy Environ. Sci. 17 (2024) 6013.

[5] T. Wallach, L. Etgar, Highly transparent and semi-transparent perovskites and their applications, Appl. Phys. Rev. 12 (2025) 011314.

[6] C. Goel, S. Yoo, Hybrid daylight harvesting system using static ball lens concentrator and movable optical fiber, Sol. Energy 216 (2021) 121.

[7] F. Polito, G. Huang, C.N. Markides, A building-integrated hybrid photovoltaic-thermal (PV-T) window for synergistic light management, electricity and heat generation, Adv. Sci. 12 (2025) 2408057.

[8] L. Wang, Y. Li, A. Bera, C. Ma, F. Jin, K. Yuan, W. Yin, A. David, W. Chen, W. Wu, W. Prellier, S. Wei, T. Wu, Device performance of the mott insulator $LaVO_3$ as a photovoltaic material, Phys. Rev. Appl. 3 (2015) 064015.

[9] A. Cheikh, A. David, U. Lüders, J. Cardin, C. Labbé, S. Duprey, D. Kumar, A. Pautrat, W. Prellier, A. Fouchet, Investigation of optical transitions and electrical properties in $LaVO_3/SrTiO_3$ heterostructure, Mater. Sci. Semicond. Process. 169 (2024) 107852.

[10] H.-T. Zhang, M. Brahlek, X. Ji, S. Lei, J. Lapano, J.W. Freeland, V. Gopalan, R. Engel-Herbert, High-quality $LaVO_3$ films as solar energy conversion material, ACS Appl. Mater. Interfaces 9 (2017) 12556.

[11] D.H. Jung, J.W. Hwang, J.J. Lee, D.H. Shin, H. Lee, High-performance and high-stability $LaVO_3$/Si solar cells through employing thickness-controlled $LaVO_3$ and a titanium oxide passivation layer, J. Alloys Compd. 904 (2022) 163818.

[12] D.H. Kim, D.H. Shin, D.H. Jung, S.D. Oh, E.J. Kim, H. Lee, Highly stable semitransparent solar cell employing graphene/WS_2/$LaVO_3$ vertical-heterostructure, J. Mater. Chem. C 12 (2024) 2843.

[13] Y. Qi, M. Almtiri, H. Giri, S. Jha, G. Ma, A.K. Shaik, Q. Zhang, N. Pradhan, X. Gu, N. I. Hammer, D. Patton, C. Scott, Q. Dai, Evaluation of the passivation effects of PEDOT:PSS on inverted perovskite solar cells, Adv. Energy Mater. 12 (2022) 2202713.

[14] S. Chen, L. Liang, Y. Zhang, K. Lin, M. Yang, L. Zhu, X. Yang, L. Zang, B. Lu, PEDOT:PSS-based electronic materials: preparation, performance tuning, processing, applications, and future prospect, Prog. Polym. Sci. 166 (2025) 101990.

[15] Z. Gao, T. Gao, Q. Geng, G. Lin, Y. Li, L. Chen, M. Li, Improving light absorption of active layer by adjusting PEDOT:PSS film for high efficiency Si-based hybrid solar cells, Sol. Energy 228 (2021) 299.

[16] X. Zhang, D. Yang, Z. Yang, X. Guo, B. Liu, X. Ren, S. Liu, Improved PEDOT:PSS/c-Si hybrid solar cell using inverted structure and effective passivation, Sci. Rep. 6 (2016) 33048.

[17] X. Yang, M. Luo, Q. Zhang, H. Huang, Y. Yao, Y. Yang, Y. Li, W. Cheng, P. Li, Simultaneously enhancing the efficiency and stability of perovskite solar cells by using P3HT/PEDOT:PSS as a double hole transport layer, Nanomaterials 14 (2024) 1476.

[18] J. Cameron, P. Skabara, The damaging effects of the acidity in PEDOT:PSS on semiconductor device performance and solutions based on non-acidic alternatives, J. Mater. Horiz. 7 (2020) 1759.

[19] H.-T. Chien, F. Pilat, T. Griesser, H. Fitzek, P. Poelt, B. Friedel, Influence of environmentally affected hole-transport layers on spatial homogeneity and charge-transport dynamics of organic solar cells, ACS Appl. Mater. Interfaces 10 (2018) 10102.

[20] T. Wu, X.-L. Shi, Y.-Y. Deng, Y.-M. Liu, M. Zhu, W.-D. Liu, M. Li, F. Yue, P. Huang, Z.-G. Chen, Q. Liu, Incorporating graphene quantum dots boosts thermoelectric performance of PEDOT:PSS films, Chem. Eng. J. 506 (2025) 160219.

[21] P. Fu, J.-K. Xiao, J.-Z. Gong, Y. Zhu, J.-A. Yao, Y.-F. Zhang, S.-G. Wang, Z.-D. Lin, F.-P. Du, Interfacial enhancement effect of graphene quantum dots on PEDOT:PSS/single-walled carbon nanotubes thermoelectric materials, Synth. Met. 280 (2021) 116861.

[22] W. Li, N. Cheng, Y. Cao, Z. Zhao, Z. Xiao, W. Zi, Z. Sun, Boost the performance of inverted perovskite solar cells with PEDOT:PSS/graphene quantum dots composite hole transporting layer, Org. Electron. 78 (2020) 105575.

[23] D.H. Shin, S.H. Shin, S. Kim, S.-H. Choi, High-performance and -stability graphene quantum dots-mixed conducting polymer/porous Si hybrid solar cells with titanium oxide passivation layer, Nanotechnology 31 (2020) 095202.

[24] C. Celindano, E. Haye, S. Bruyère, P. Boulet, A. Boileau, S. Migot, S. Mathieu, P. Miska, S. Barrat, F. Capon, Probing the growth window of $LaVO_3$ perovskites thin films elaborated using magnetron co-sputtering, Ceram. Int. 45 (2019) 16658.

[25] F.A. Permatasari, A.H. Aimon, F. Iskandar, T. Ogi, K. Okuyama, Role of C–N configurations in the photoluminescence of graphene quantum dots synthesized by a hydrothermal route, Sci. Rep. 6 (2016) 21042.

[26] R. Das, S. Parveen, A. Bora, P.K. Giri, Origin of high photoluminescence yield and high SERS sensitivity of nitrogen-doped graphene quantum dots, Carbon 160 (2020) 273.

[27] C.W. Jang, D.H. Shin, S.-H. Choi, Highly-flexible and -stable deep-ultraviolet photodiodes made of graphene quantum dots sandwiched between graphene layers, Dyes Pigm 163 (2019) 238.

[28] D.H. Shin, S.W. Seo, J.M. Kim, H.S. Lee, S.-H. Choi, Graphene transparent conductive electrodes doped with graphene quantum dots-mixed silver nanowires for highly-flexible organic solar cells, J. Alloys Compd. 744 (2018) 1.

[29] S.H. Kim, Control of the charge carrier concentration and hall mobility in PEDOT:PSS thermoelectric films, Bull. Kor. Chem. Soc. 38 (2017) 1460.

[30] J.C. Yu, J.A. Hong, E.D. Jung, D.B. Kim, S.-M. Baek, S. Lee, S. Cho, S.S. Park, K. J. Choi, M.H. Song, Highly efficient and stable inverted perovskite solar cell employing PEDOT:GO composite layer as a hole transport layer, Sci. Rep. 8 (2018) 1070.

[31] Y.-J. Lin, F.-M. Yang, C.-Y. Huang, W.-Y. Chou, Increasing the work function of poly(3,4-ethylenedioxythiophene) doped with poly(4-styrenesulfonate) by ultraviolet irradiation, Appl. Phys. Lett. 91 (2007) 092127.

[32] J.-S. Yeo, J.-M. Yun, D.-Y. Kim, S. Park, S.-S. Kim, M.-H. Yoon, T.-W. Kim, S.-I. Na, Significant vertical phase separation in solvent-vapor-annealed poly(3,4-ethylenedioxythiophene):poly(styrene sulfonate) composite films leading to better conductivity and work function for high-performance indium tin oxide-free optoelectronics, ACS Appl. Mater. Interfaces 4 (2012) 2551.

[33] J.C. Yu, J.I. Jang, B.R. Lee, G.-W. Lee, J.T. Han, M.H. Song, Highly efficient polymer-based optoelectronic devices using PEDOT:PSS and a GO composite layer as a hole transport layer, ACS Appl. Mater. Interfaces 6 (2014) 2067.

[34] S. Kim, S.W. Hwang, M.-K. Kim, D.Y. Shin, D.H. Shin, C.O. Kim, S.B. Yang, J. H. Park, E. Hwang, S.-H. Choi, G. Ko, S. Sim, C. Sone, H.J. Choi, S. Bae, B.H. Hong, Anomalous behaviors of visible luminescence from graphene quantum dots: interplay between size and shape, ACS Nano 6 (2012) 8203.

[35] M. Saliba, L. Etgar, Current density mismatch in perovskite solar cells, ACS Energy Lett. 5 (2020) 2886.

[36] J.D. Servaites, M.A. Ratner, T.J. Marks, Organic solar cells: a new look at traditional models, Energy Environ. Sci. 4 (2011) 4410.

[37] H. Pan, H. Shao, X.L. Zhang, Y. Shen, M. Wang, Interface engineering for high-efficiency perovskite solar cells, Appl. Phys. 129 (2021) 130904.

[38] F. Mirkhosravi, A. Rashidi, A.T. Elshafiey, J. Gallagher, Z. Abedi, K. Ahn, A. Lintereur, E.K. Mace, M.A. Scarpulla, D. Feezell, Effects of fast and thermal neutron irradiation on Ga-polar and N-polar GaN diodes, J. Appl. Phys. 133 (2023) 015704.

[39] S. Batool, M. Idrees, S.-T. Han, V.A.L. Roy, Y. Zhou, Electrical contacts with 2D materials: current developments and future prospects, Small 19 (2023) 2206550.

[40] J. Chen, C. Zhang, X. Liu, L. Peng, J. Lin, X. Chen, Carrier dynamic process in all-inorganic halide perovskites explored by photoluminescence spectra, Photonics Res. 9 (2021) 151.

[41] J. Cameron, P.J. Skabara, The damaging effects of the acidity in PEDOT:PSS on semiconductor device performance and solutions based on non-acidic alternatives, Mater. Horiz. 7 (2020) 1759.

[42] J. Zhu, Y. Xu, Y. Luo, J. Luo, R. He, C. Wang, Y. Wang, K. Wei, Z. Yi, Z. Gao, J. Wang, J. You, Z. Zhang, H. Lai, S. Ren, X. Liu, C. Xiao, C. Chen, J. Zhang, F. Fu, D. Zhao, Custom-tailored hole transport layer using oxalic acid for high-quality tin-lead perovskites and efficient all-perovskite tandems, Sci. Adv. 10 (2024) eadl2063.